Ferroelectric smectic-*C** liquid-crystal phase: Reexamination of the electric-field influence

Zdravko Kutnjak*
Jožef Stefan Institute, P. O. Box 3000, 1001 Ljublijana, Slovenia
(Received 7 June 2004; revised manuscript received 26 August 2004; published 16 December 2004)

Calorimetric and dielectric experiments are presented near the recently proposed Lifshitz point in order to study the nature and properties of the newly suggested phase transitions in the electric-field-temperature (*E*-*T*) phase diagram. It was found that both calorimetric and dielectric results obtained across the recently proposed $\overline{C_1}$-$\overline{C_2}$ transition line agree with the predictions of the extended Landau model, showing that the $\overline{C_1}$-$\overline{C_2}$ transition line is not a true phase transition but is merely a continuous evolution similar to a supercritical evolution between two states possessing microscopically the same symmetry. However, it was confirmed in agreement with findings by Ghoddoussi *et al.* that in samples of finite thickness the extended Landau model cannot adequately describe some features of the *E*-*T* phase diagram and some other physical quantities such as the Goldstone mode temperature dependence and the polarization field dependence $P(E)$. These discrepancies are discussed within the frame of a relaxing mechanism of the helicoidal structure involving annihilation of pairs of $\pm 2\pi$ disclination lines.

DOI: 10.1103/PhysRevE.70.061704 PACS number(s): 61.30.Eb, 64.70.Md, 89.75.Da

I. INTRODUCTION

In 1975, Meyer *et al.* [1] discovered a ferroelectric behavior in a liquid-crystal (LC) mesophase since then known as the smectic-*C** (C^*) phase. Although the ferroelectric properties have been found later also in the chiral smectic-*I** and smectic-*F** phases, the most disordered one, the *C** phase, has attracted the most attention due to possible application for fast electro-optical switching devices [2]. The ferroelectric smectic-*C** phase is a tilted smectic-*C* (C) phase formed by orientationally ordered chiral molecules with a one-dimensional density modulation. In the high temperature paraelectric smectic-*A** (A^*) phase the molecules are stacked in smectic layers with their long axes, on average, oriented perpendicular to the layers. In a tilted *C* phase the tilt of the long molecular axis toward smectic layers breaks the axial symmetry around the long molecular axis. In the *C** phase, both the molecular tilt and perpendicular in-plane polarization rotate gradually from one smectic plane to another, thus forming a helicoidal structure with the period *p*, the pitch, and associated wave vector $q=2\pi/p$. This structure acts as a highly regular domain structure resulting in a zero net macroscopic polarization.

Due to the electric-field-polarization coupling $\vec{E}\cdot\vec{P}$ it was possible to study response of the *C** phase to an electric field via dielectric measurements, tilt angle, and spontaneous polarization measurements. It was soon discovered that the helicoidal smectic-*C** phase could be unwound into a homogeneous smectic-*C*-like ferroelectric phase (denoted as smectic-$\overline{C}$ or $\overline{C}$) by applying an electric field above some threshold critical value E_C. The temperature dependence of the electric critical field $E_C(T)$ has been measured by many research groups [3–9]. The $E_C(T)$ line plays the role of a phase boundary between the helicoidal *C** and unwound $\overline{C}$ in an electric-field-temperature (*E*-*T*) phase diagram. One such example is the *E*-*T* phase diagram of *p*-decyloxybenzylidene *p′*-amino 2-methylpentylcinnamate (DOBA-1-MPC) shown as open circles in Fig. 1. For symmetry reasons the smectic-*A* phase exists only on the ordinate axis above T_C; namely, already a small electric field induces a tilt angle, thus inducing the homogeneous $\overline{C}$ phase. The helicoidal *C** phase is contained below the $E_C(T)$ line denoted by open circles.

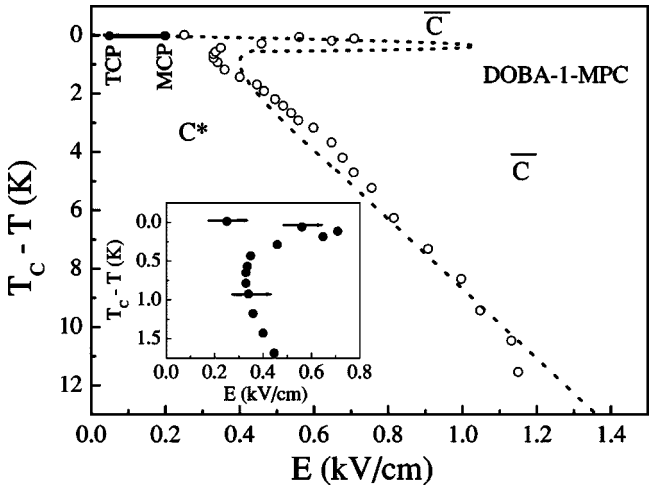

FIG. 1. *E*-*T* phase diagram of DOBA-1-MPC. Open circles represent polarization microscope observations of the critical field $E_C(T)$ at which the helicoidal structure completely unwinds [9,10]. The direction of approach to the unwound $\overline{C}$ phase was along the field axis as denoted by arrows in the inset showing in detail the temperature range near T_C. Specifically, the temperature was kept constant and the electric field was increased until the helicoidal pitch structure disappeared. Dashed and solid lines are second and first order transition lines, respectively, predicted by the generalized model [11,12]. The predicted locations of the tricritical and multicritical points are denoted by TCP and MCP, respectively.

*URL: http://www2.ijs.si/~kutnjak

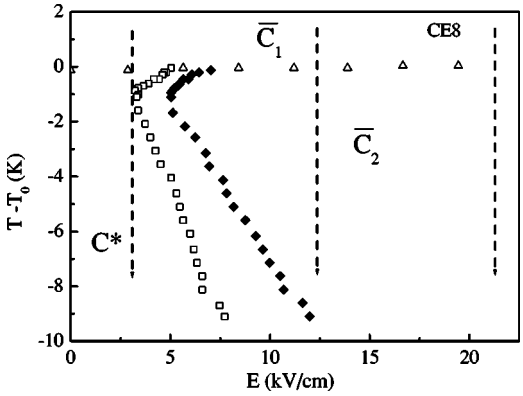

FIG. 2. *E-T* phase diagram of CE8 [18]. According to [18] open triangles represent the second order transition line between either two homogenous smectic $\overline{C}_1$ and $\overline{C}_2$ phases which differ in symmetry or between the homogeneous $\overline{C}_1$ phase and the helicoidal smectic-*C** phase. These two cases are separated by the tricritical Lifshitz point, which should be positioned somewhere near the point where the first order line (denoted by diamonds or squares for increasing and decreasing fields, respectively) separating the helicoidal smectic-*C** phase and the homogeneous $\overline{C}_2$ phase meets the abovementioned second order line (denoted by open triangles). The dashed arrows indicate electric fields at which the CE8 was studied using high resolution calorimetry in this work.

So far it has been the general consensus that the physical properties, including the *E-T* phase diagram, could qualitatively be well described by the extended phenomenological model based on a generalized Landau expansion [13], which superseded some earlier attempts based on more simple Landau models [14–16]. Among these, the temperature and electric-field dependences of the soft and Goldstone dielectric susceptibility modes, heat capacity, pitch, polarization, and tilt could all supposedly be qualitatively well described within the generalized Landau model (GLM) [13,17]. In addition, the generalized model prediction of the *E-T* phase diagram appeared also to agree qualitatively well with the published experimental results [11,12]. In fact, the GLM predicted two smectic ferroelectric phases distinctive in symmetry, the *C** and *C* phases separated by the transition line $E_C(T)$ on which tricritical (TCP) and multicritical (MCP) points could be found (see dashed and solid lines in Fig. 1).

Very recently, however, optical experiments by Ghoddoussi *et al.* [18] obtained on S-(+)-[4-(2′-methylbutyl) phenyl 4′-*n*-octylbiphenyl-4-carboxylate] (CE8) suggested a new *E-T* phase diagram of a ferroelectric *C** liquid crystal incompatible with all existing theoretical models in which two second order lines and one first order line meet at a Lifshitz tricritical point (Fig. 2). It was also proposed that at larger electric fields a second order line separates two distinctive helix free "unwound" phases $\overline{C}_1$ and $\overline{C}_2$, which differ perhaps in the tilt orientation. This picture is basically similar to what was found in the case of the magnetic-field-temperature phase diagram (*B-T*) of ferroelectric liquid crystals [19].

Since the above *E-T* phase diagram proposed by Ghoddoussi *et al.* [18] cannot be explained within the established theoretical models it calls for additional experimental investigation. In order to learn more about transition lines in the *E-T* phase diagram several experiments were carried out across the $\overline{C}_1$ to $\overline{C}_2$ and the *C** to $\overline{C}_2$ transition lines. Specifically, the nature of the newly proposed phase transition between two homogeneous smectic $\overline{C}_1$ and $\overline{C}_2$ phases was studied by high resolution calorimetry on CE8 (Sec. II) at various electric fields in the vicinity of the proposed Lifshitz point (denoted by dashed arrows in Fig. 2). Furthermore, high resolution dielectric experiments (Sec. II) were conducted in order to check the existence of any small sharp anomaly in the dielectric susceptibility χ associated with the $\overline{C}_1$ to $\overline{C}_2$ transition line. In addition to this, the evolution of several physical parameters such as the electric-field dependence of the dielectric polarization was verified across the *C** to $\overline{C}_2$ transition line (Secs. III and IV). Finally, the experimental results are discussed in the light of some other inconsistencies between the experimental results obtained in smectic-*C** systems and the theoretical models (Sec. IV).

II. INVESTIGATIONS ACROSS $\overline{C}_1$-*C** AND $\overline{C}_1$-$\overline{C}_2$ TRANSITION LINES

A. Calorimetric investigations

1. Experimental setup

The ferroelectric chiral liquid crystal compound S-(+)-[4-(2′-methylbutyl) phenyl 4′-*n*-octylbiphenyl-4-carboxylate] (denoted as CE8 or 8SI*) with the following cooling phase sequence (obtained from the bulk CE8 calorimetric run)

$$\text{Cryst} \underset{313\ ^\circ\text{C}}{\leftrightarrow} \text{G}^* \underset{336.5\ ^\circ\text{C}}{\leftrightarrow} \text{J}^* \underset{338.2\ ^\circ\text{C}}{\leftrightarrow} \text{I}^* \underset{340.2\ ^\circ\text{C}}{\leftrightarrow} \text{C}^* \underset{358.0\ ^\circ\text{C}}{\leftrightarrow} \text{A}^*$$

$$\underset{406.1\ ^\circ\text{C}}{\leftrightarrow} \text{N}^* \underset{412.1\ ^\circ\text{C}}{\leftrightarrow} \text{BPI} \underset{415.6\ ^\circ\text{C}}{\leftrightarrow} \text{BPII}\,? \underset{416.1\ ^\circ\text{C}}{\leftrightarrow} \text{BPIII} \underset{417.7\ ^\circ\text{C}}{\leftrightarrow} \text{Iso}$$

was filled in the sample cell consisting of two planparallel silver foil sheets separated by a 230 μm thick Mylar spacer. The silver foils served also as electrodes in order to apply an electric bias field.

Heat-capacity data were acquired by a computerized calorimeter. Description of the technique was extensively given in Refs. [20,21]. The calorimeter is capable of automated operation in either ac or relaxation mode. The sample, which is contained in a sealed silver cell, is thermally linked to a temperature-stabilized bath (within 0.1 mK) by support wires and by air. The thermal link can be represented by a thermal resistivity of $R_T \sim 220$ near the transition temperature to the *C** phase.

During the calorimetric investigation no presence of latent heat was detected so we focus only on the high-resolution ac experiments.

The data were taken on cooling the sample either from the *A** or the $\overline{C}_1$ phase with the cooling rate of 100 mK/h in the vicinity of the transition to the *C** or $\overline{C}_2$ phase and of 300 mK/h further away from the transition. The typical amplitude of T_{ac} was about 20 mK. The heat capacity of the empty cell was later subtracted from the heat-capacity data. The net heat capacity $C(T)$ so obtained was divided by the mass of the CE8 sample (19.9 mg) in order to obtain the

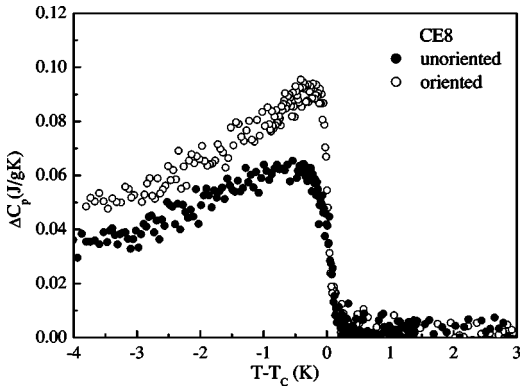

FIG. 3. Temperature dependence of the excess heat capacity data $\Delta C_p(T)$ for unoriented sample (solid circles) and oriented sample (open circles). Note the much sharper and larger heat-capacity anomaly in the case of the oriented sample.

specific heat capacity C_p in J/g K. The excess heat capacity associated with some particular transition can be defined by

$$\Delta C_p = C_p(T) - C_p(\text{baseline}), \tag{1}$$

where C_p(baseline) represents C_p variations expected in the absence of a particular phase transition.

The specific heat was first measured in zero electric field on the unoriented sample and then on the bookshelf geometry oriented sample with the smectic layers perpendicular to the electrodes (Fig. 3). The details of the orienting procedure are given in Refs. [22,23]. In our case, the sample cell was exposed to the magnetic field of strength 9 T in the nematic phase just above the nematic to A^* transition. Then it was slowly cooled down to $\approx$10 K above the A^* to C^* transition. Here, the cell was removed from the magnetic field and exposed for several hours to the static electric bias field of $\approx$20 kV/cm in order to account for some additional adjustment and reorientation to the electric ordering field and transient ionic current effects. After that, the bias electric field was removed and the specific heat was measured again repeatedly at various values of the dc bias electric field.

As shown in Fig. 3, the oriented-sample excess heat-capacity ΔC_p anomaly is much sharper and about 50% larger than that of the unoriented sample. This could be a consequence of the formation of focal conic domains in the unoriented sample, which could be seen as a source of additional defects and pinning sites. It should be noted that the shape of the ΔC_p anomaly of the oriented sample remained unchanged even after several successive zero-field cooling and heating runs within a week's time. These zero-bias-field ΔC_p results of the oriented sample were later compared to the results obtained in nonzero-bias-field runs.

2. Experimental results

Before discussing the calorimetric results let us review first the predictions of the generalized Landau model [13,17]. The free-energy density in the absence of an external electric field could be written as [13]

$$\begin{aligned} g_0(z) = {} & \frac{1}{2}a|\vec{\xi}|^2 + \frac{1}{4}b|\vec{\xi}|^4 + \frac{1}{6}c|\vec{\xi}|^6 - \Lambda\left(\xi_1\frac{d\xi_2}{dz} - \xi_2\frac{d\xi_1}{dz}\right) \\ & + \frac{1}{2}K_3\left|\frac{d\vec{\xi}}{dz}\right|^2 - d|\vec{\xi}|^2\left(\xi_1\frac{d\xi_2}{dz} - \xi_2\frac{d\xi_1}{dz}\right) + \frac{1}{2\epsilon}|\vec{P}|^2 \\ & + \frac{1}{4}\eta|\vec{P}|^4 - \mu\vec{P}\cdot\frac{d\vec{\xi}}{dz} + C(P_x\xi_2 - P_y\xi_1) \\ & - \frac{1}{2}\Omega(P_x\xi_2 - P_y\xi_1)^2. \end{aligned} \tag{2}$$

Here, $\vec{\xi}=\xi_1\hat{x}+\xi_2\hat{y}$ denotes the two-component tilt vector order parameter with its absolute value approximately equal to the tilt angle $|\vec{\xi}|\approx\theta$ and $\vec{P}=P_x\hat{x}+P_y\hat{y}$ denotes the two-component in-plane polarization vector order parameter. The coordinate system is chosen so that the z axis is perpendicular to the smectic planes, i.e., parallel to the helicoidal axis. In the presence of an external electric field two additional terms should be added to the g_0,

$$g(z) = g_0(z) - \vec{E}\cdot\vec{P} - \frac{\varepsilon_0(\varepsilon_\parallel - \varepsilon_\perp)}{2}(\vec{\xi}\cdot\vec{E})^2. \tag{3}$$

The last term, quadratic in $\vec{E}$, was usually neglected in the case of ferroelectric liquid crystals since it remains typically more than two orders of magnitude smaller than the linear term even if the most favorable combination of the known physical parameters is chosen, i.e., small polarization and large dielectric anisotropy $\varepsilon_\parallel - \varepsilon_\perp$ and tilt.

The excess heat capacity could be calculated according to its definition

$$\Delta C_p = -T\left(\frac{d^2g}{dT^2}\right)_p. \tag{4}$$

In order to calculate the heat capacity the material parameters were roughly estimated by either fitting some known physical quantities such as temperature dependence of the soft and Goldstone modes [23], tilt angle θ [18], and zero-field heat-capacity anomaly (Fig. 3) or approximately matching the value of the pitch [18]. It was found that the relative magnitude and sign of the material parameters resemble closely the published set of material parameters for 2-methylbutyl 4-(4-decyloxybenzylideneamino)cinnamate (DOBAMBC) [17].

Figure 4 shows the temperature dependence of the heat capacity calculated at several values of the bias electric field E, which was applied parallel to the smectic planes, i.e., the same geometry as in the actual experiment.

According to the GLM model, the ordering effect of the electric field (electroclinic effect) induces both tilt and polarization well above the $T_C(E=0)$, i.e., at sufficiently high values of the electric field the state above and below $T_C(E=0)$ possesses the same symmetry and the sharp transition vanishes, changing its nature to a gradual continuous conversion from the high-temperature state with low values of the order parameters to the low-temperature state with larger values of the order parameters. Consequently, the high-temperature heat-capacity wing becomes stronger with increasing field E

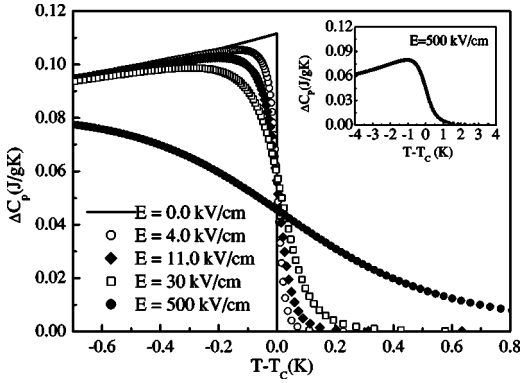

FIG. 4. Predictions of the generalized Landau model for the temperature dependence of the excess heat capacity $\Delta C_p(T)$ calculated at several electric-field values. The inset shows $\Delta C_p(T)$ in a wider temperature range calculated at $E=500$ kV/cm.

and the heat-capacity anomaly itself becomes wider and suppressed with increasing field. This is especially visible for the curve (also shown in a wider temperature range in the inset to Fig. 4) calculated at a very high value of the electric field $E=500$ kV/cm, actually well above physically accessible values of $E\approx 50$ kV/cm.

The position of the anomaly itself is also slightly shifted toward higher temperatures (<20 mK at $E=30$ kV/cm). Such small shifts are very difficult to detect reliably in experiments because of the anomalous shift of T_C with time ($\sim 20-40$ mK/run, run time about 4–5 days) due to slow electrochemical degradation of the sample. Due to this and partly for clarity, all calculated curves in Fig. 4 as well as experimental heat-capacity data (Fig. 5) were shifted in temperature so that they match at half of the peak value on the high-temperature side of the anomaly. Figure 5 shows in three panels a pairwise comparison between the heat-capacity data of the oriented bulk in zero electric field and the heat-capacity obtained at $E=3.03$, 12.27, and 21.37 kV/cm from top to bottom.

Qualitative agreement could be found within the experimental error between the experimental results and generalized Landau model theoretical predictions; namely, by comparing Figs. 4 and 5, both systematic enhancement of the pretransitional wing and the widening of the heat-capacity anomaly could be observed in the experimental data with increasing electric field (open circles). It should be noted that well agreement could be found in the range of electric fields where the second order transition should be expected between the $\overline{C_1}$ and $\overline{C_2}$ homogeneous phases.

B. Dielectric investigations

One can argue that the heat-capacity anomaly is rather small and that the field-induced effects in heat-capacity data are not large enough to serve as a convincing proof that the GLM predictions are correct. Fortunately, there is another physical quantity which exhibits a sharp anomaly at T_C, namely, dielectric susceptibility associated with the soft mode fluctuations $\chi=\varepsilon-1$. As shown in this section, χ shows much more significant electric-field dependence than the heat

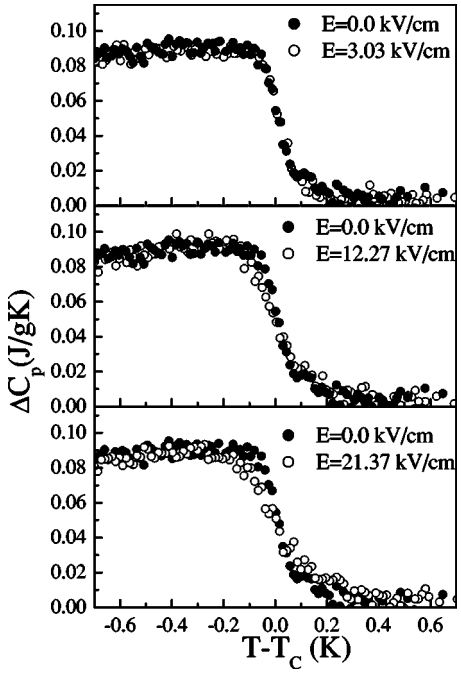

FIG. 5. Pairwise comparison between the temperature dependence of the heat capacity obtained in zero electric field and temperature dependences obtained in (top to bottom) $E=3.03$, 12.27, and 21.37 kV/cm.

capacity and could thus serve as a probe to provide information about the nature of the $\overline{C_1}$ to $\overline{C_2}$ transition line.

1. Experimental setup

The complex dielectric constant $\varepsilon^*(T,\omega)=\varepsilon'-i\varepsilon''$ was measured by using a HP4282A precision *LCR* meter. The method was described in Refs. [22,23]. The liquid crystal was confined within a glass cell of thickness $d\sim 50$ μm. The plane parallel glass plates were covered by indium tin oxide electrodes. The samples were oriented in the same way as in the case of heat-capacity measurements, i.e., by exposing the sample to the magnetic field of strength 9 T on cooling the sample through the isotropic to nematic transition. The smectic layers were stacked in the so-called bookshelf arrangement so that smectic planes were perpendicular to the electrode planes. In this geometry the vector of the electric field is parallel to the smectic planes. The amplitude of the excitation ac voltage was kept below 1 V.

In scanning runs the dielectric constant was measured at a few frequencies between 40 Hz and 4 kHz on cooling the sample with the typical cooling rate of 200 mK/h in the various dc bias electric fields.

2. Dielectric susceptibility results

Again, before discussing the dielectric susceptibility results let us review first the predictions of the generalized Landau model. It was shown within the GLM (3) that the dielectric susceptibility response

$$\chi=\lim_{E\to 0}\frac{\langle P\rangle}{E} \tag{5}$$

could be divided into two modes, one associated with the amplitude changes (soft mode χ_s) and one that is due to

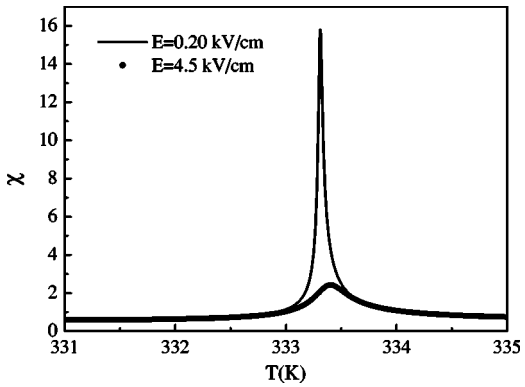

FIG. 6. Temperature dependence of the soft mode susceptibility according to calculations based on the generalized Landau model for two different electric-field values. Note the strong suppression and gradual evolution of the anomaly calculated at $E=4.5$ kV/cm well above $E_C \approx 0.6$ kV/cm.

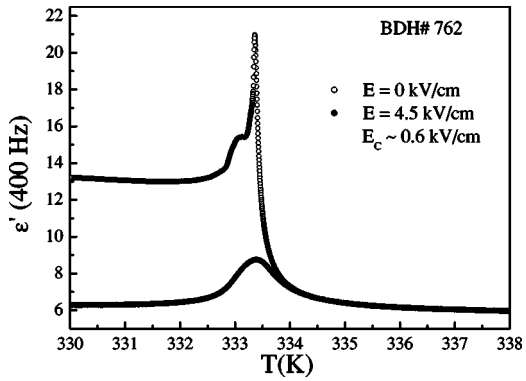

FIG. 7. Dielectric susceptibility measured at two different values of the static bias electric field of the ferroelectric liquid crystal compound with large spontaneous polarization. The sharp anomaly at ≈333.3 K (open circles) corresponds to the critical peak of the soft mode susceptibility. Note strong suppression and gradual evolution of the χ_s anomaly (solid circles) measured at $E=4.5$ kV/cm well above $E_C \approx 0.6$ kV/cm.

phase changes (Goldstone mode χ_G) of the order parameter $\vec{\xi}$ [17]. The soft mode is critical

$$\chi_s \propto (T - T_C)^{-\gamma}, \tag{6}$$

with critical exponent $\gamma=1$ according to the GLM. The Goldstone mode appears below T_C and with its typically much larger intensity obscures the soft mode below T_C, making the latter very difficult to detect.

Since the intensity of the soft mode in CE8 is rather small even in zero-bias electric field, as shown in Ref. [23], the dielectric investigations were performed for the sake of convenience on ferroelectric mixtures with large spontaneous polarization (BDH Ltd. catalog number 762). The material parameters in our calculations were slightly modified in order to accommodate different T_C values, the dielectric susceptibility intensities, and the critical field value of $E_C \approx 0.6$ kV/cm.

Figure 6 shows calculation of the soft mode susceptibility based on the GLM for two different values of the static bias electric field. As in the case of the heat capacity, the sharp χ anomaly calculated at low bias electric field ($E<E_C$) (solid line in Fig. 6) converts to a rather strongly suppressed and gradually changing anomaly (solid circles in Fig. 6) at fields well above E_C. Here, the small value of the electric field $E=0.2$ kV/cm was chosen in order to accommodate the convoluting effect of the small ac measuring field in the case of the zero-bias-field dielectric experiment shown in Fig. 7.

Figure 7 shows the dielectric susceptibility measured in the ferroelectric mixture with large spontaneous polarization, BDH762. A comparison is made between the dielectric data obtained in the zero-bias electric field (open circles) and in the static bias electric field above critical field $E \gg E_C$ (solid circles). The deviations below $T_C \approx 333.3$ K in the case of the zero-field data from the theory-predicted behavior (Fig. 6) are due to the superimposed Goldstone mode contribution (which was omitted in Fig. 6). With the bias electric field above E_C the Goldstone mode indeed completely disappears, as shown before [24], and the only contribution observed in the dielectric susceptibility is of the soft mode. The experimental results in Fig. 7 seem to match completely the generalized Landau model predictions shown in Fig. 6. Within the experimental resolution better than 0.001%, there seems to be no evidence for any even very small sharp anomaly related to the second order transition between $\overline{C}_1$ and $\overline{C}_2$ phases. It should be noted that the above findings are in agreement with findings obtained on a room-temperature ferroelectric liquid crystal compound reported some time ago [25].

So far we have been focused only on the transition line in the E-T phase diagram separating either $\overline{C}_1$ from C^* phase or $\overline{C}_1$ from proposed $\overline{C}_2$ phase. Let us focus in the next section on the transition line separating C^* from $\overline{C}$ phase.

III. POLARIZATION REVERSAL INVESTIGATIONS ACROSS THE C^*-$\overline{C}$ TRANSITION LINE

The C^* to $\overline{C}$ transition line was typically determined by optical measurements of the critical value of the electric bias field E at which the helicoidal pitch $p(E)$ diverges. As shown by Ghoddoussi *et al.* [18], the field dependence of the C^* to $\overline{C}$ transition line measured in CE8 and several other liquid crystal compounds (including DOBA-1-MPC) does not agree well with the predictions of the GLM, especially so in the narrow temperature range just below T_C (Fig. 1). In order to verify further the predictions of the generalized Landau model about the field evolution of physical quantities across the C^* to $\overline{C}$ transition line the dielectric polarization $P(E)$, i.e., polar ordering $P(E) \propto \langle \cos \phi \rangle (E)$, was studied as a function of the electric field via measurements of the polarization reversal current I_P.

A. Experimental setup

The electric-field dependence of the dielectric polarization $P(E)$ was measured via measurements of the polarization reversal current. The method was described in detail in Refs.

[26,27]. Here, a bipolar square-wave voltage was applied and the induced current I was measured through the sample cell. After subtraction of the other current contributions not connected to polarization switching, such as the capacitor relaxation current contribution, ionic current contribution, and electroclinic current contribution, the polarization was obtained by integrating the remaining "bump" in the polarization reversal current I_P,

$$P = \frac{1}{2S} \int I_P(t) dt. \tag{7}$$

Here, S denotes the area of the electrodes. By varying the amplitude of the square-wave voltage one could obtain $I_P(E,t)$ and consequently $P(E)$. The frequency of the square-wave voltage was kept low enough to allow the sample to reach equilibrium after each polarization reversal sequence.

As shown by Dahl *et al.* [26], in the case of polarization reversal current experiments, the dielectric polarization $P(E)$ can be considered as a measure of the polar ordering $\langle \cos \phi \rangle(E)$,

$$P(E) = P_S(T,E)\langle \cos \phi \rangle(E) = \frac{1}{2S} \int I_P(t) dt, \tag{8}$$

where $P_S(T,E)$ denotes the amplitude of the polarization vector at a particular temperature and field, and ϕ denotes the angle between the in-plane polarization vector $\vec{P}$ and the vector of the external bias field $\vec{E}$ [see also text related to Eq. (7)]. Since the angle ϕ changes from one smectic plane to another, $\cos \phi$ should be averaged over the period of the helicoidal structure, i.e., over the pitch distance (denoted by $\langle\ \rangle$). Because the current reversal experiment is performed on samples with typical length much larger than the pitch, the integrated current response is proportional to the averaged $\langle \cos \phi \rangle$. In the limit of small electric fields $P_S(T,0)$ is equal to the spontaneous polarization P_S. At larger electric fields and deeper in the smectic-C^* phase, the temperature dependence of $P_S(T,E)$ (mainly due to the electroclinic effect) can be approximated to the lowest terms $P_S(T,E) \approx P_S(T,0) + \epsilon(T)E$.

B. Polarization reversal results

Figures 8(a) and 8(b) show the electric-field dependence of the dielectric polarization $P(E)$ at two different temperatures below the A to C^* transition. Here, DOBA-1-MPC was found to be a better choice to study than CE8 since the spontaneous polarization of the former exceeds by an order of magnitude the P_S of CE8, yet its phase diagram is equally well studied as that of CE8 (Fig. 1).

For both temperatures the $P(E)$ data could be separated apparently into two electric-field ranges with nearly linear behavior. In the first range $P(E)$ increases nearly linearly, and then exhibits crossover to another linear regime with much smaller slope. Note that the linear increase at low electric fields exhibits small acceleration roughly in the middle of the first linear regime.

Before proceeding let us recall what are the theoretical predictions for the electric-field dependence of the polar ordering $\langle \cos \phi \rangle(E)$. The solid line in Fig. 9 represents the theoretical calculation of the polar ordering $\langle \cos \phi \rangle(E)$ based on the GLM [28]. The calculated polar ordering $\langle \cos \phi \rangle(E)$ also increases nearly linearly at lower fields, but in striking contrast to the $P(E)$ data in Figs. 8(a) and 8(b) the bulk of its rise to its saturated value at E_C happens in the last 5% of the E/E_C range.

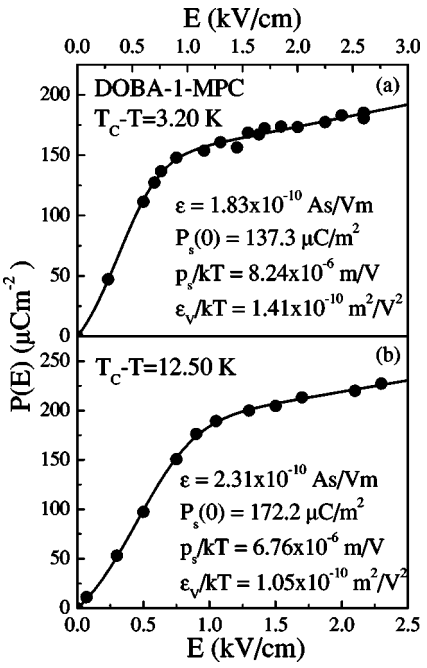

FIG. 8. Dielectric polarization $P(E)$ (solid circles) as a function of the bias electric field E measured 3.2 K below T_C (a) and 12.5 K below T_C (b). Solid lines in both panels represent fits to the activated domain switching ansatz (see text for explanation of fitting parameters).

Strictly speaking, the $P(E)$ data in Fig. 8 do not represent directly the polar ordering $\langle \cos \phi \rangle(E)$. In order to get $\langle \cos \phi \rangle(E)$ the $P(E)$ data should be divided by the amplitude of the polarization vector $P_s(T,E)$, i.e., $\langle \cos \phi \rangle(E) = P(E)/[P_S(T) + \epsilon(T)E]$.

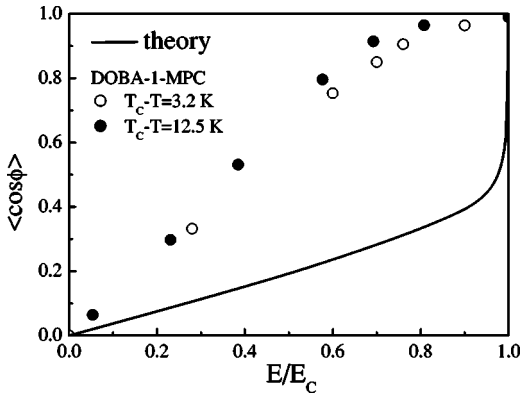

FIG. 9. Reduced electric-field dependence of the polar ordering $\langle \cos \phi \rangle(E)$. Solid line denotes calculation based on the generalized Landau model [28], while open and solid circles represent experimental data obtained via measurements of $P(E)$.

Solid and open circles in Fig. 9 denote experimentally determined $\langle \cos \phi \rangle(E)$ after the $P(E)$ data were divided by $P_s(T,E) = P_S(T) + \epsilon(T)E$. It is evident that the field dependence of the polar ordering $\langle \cos \phi \rangle(E)$ across the C^* to $\overline{C}$ transition line differs significantly from the theoretical calculations based on the generalized Landau model. Here, $P_S(T)$ and $\epsilon(T)$ were determined by fitting the linear $P(E)$ dependence at higher electric fields, i.e., in the second linear regime. It should be noted that the spontaneous polarization P_S values so obtained match well previously published data [22] obtained in the classical fashion by studying the polarization hysteresis loops.

It is interesting to note that $P(E)$ curves could be well described [see solid lines and listed fit parameters in Figs. 8(a) and 8(b)] by the "activated domain switching" expression

$$P(E) = P_S(T,E)\tanh\left(\frac{p_S(T,E)E}{kT}\right), \tag{9}$$

in which the ferroelectric domain reverses its polarization by flipping across some energy barrier via an activated process. Here $p_S(T,E) = p_S(T,0) + \epsilon_V(T)E$ represents the local dipolar moment and $P_S(T,E) \approx P_S(T,0) + \epsilon(T)E$ denotes the polarization as defined above.

IV. DISCUSSION

Calorimetric and dielectric investigations presented in Sec. II across the $\overline{C}$ to C^* and newly proposed $\overline{C_1}$ to $\overline{C_2}$ transition lines seem to corroborate the predictions of the generalized Landau model about the latter; namely, excellent agreement could be found within the experimental error between the calorimetric, dielectric, and tilt angle [18] experimental results and the calculations based on the GLM (compare Figs. 4 and 5 as well as Figs. 6 and 7) at the electric fields where the second order transition was proposed between the $\overline{C_1}$ and the new $\overline{C_2}$ homogeneous phase. The slow gradual conversion, i.e., lack of sharp anomalies in the heat capacity and the dielectric response at higher electric fields, seems to support the original scenario in which the electric field above the critical unwinding electric field induces a state with the same symmetry at all temperatures, which gradually converts toward the low-temperature state with increasingly larger order parameters. In fact, according to the GLM and the experimental results the order parameters vary with the strongest rate at the proposed $\overline{C_1}$ to $\overline{C_2}$ transition line. Consequently, physical quantities such as C_p and χ exhibit a broad anomaly at the same line. Therefore, it seems that for the electric fields studied the $\overline{C_1}$ to $\overline{C_2}$ transition line does not represent a new transition line between two phases, but merely a locus of the strongest otherwise gradual nonsingular variation in properties within the same phase $\overline{C}$ (see dashed line in Fig. 10), similar to the locus of the gradual supercritical conversion in a simple fluid above the liquid-gas critical pressure. It should also be stressed that so far there is no experimental evidence, which would confirm the existence of the first order line section between TCP and MCP in the $\overline{C}$ to C^* transition line; namely, heat-capacity results and dielectric results at several electric fields below E_C (not shown here) do not indicate the existence of latent heat.

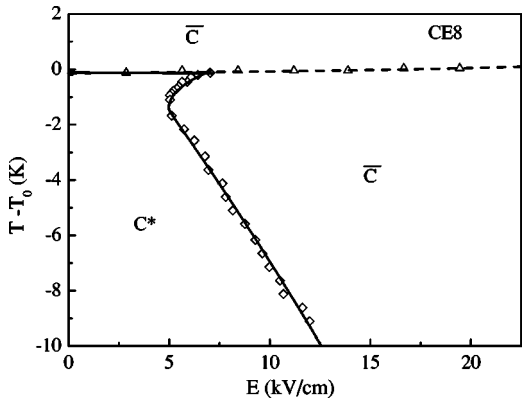

FIG. 10. E-T phase diagram of CE8 [18]. Dashed line represents the locus of the strongest otherwise nonsingular variation in properties within the same phase $\overline{C}$. Solid line denotes the limits of the C^* phase.

It should be noted, however, that the above results do not completely exclude the existence of a $\overline{C_2}$ phase. In fact, a recent theoretical effort [29] indicates that by taking into account the quadratic term the $\overline{C_2}$ phase would be contained in the portion of the E-T phase diagram at very large electric fields if calculated for a realistic set of material parameters. It is not yet clear whether that region is experimentally accessible due to possible breakdown of the sample. Anyway, so far there is no experimental evidence that would support its existence as well as the existence of the tricritical Lifshitz point in the E-T phase diagram of ferroelectric liquid crystals.

As shown in [18], the generalized Landau model has some difficulties in describing in detail the E-T phase diagram. Two apparent problems can be readily identified: (i) the $E_C(T)$ at larger $T - T_C$ values seems to follow rather a square-root dependence than a nearly linear dependence on $T - T_C$ [18] and (ii) the very shape of the sharp cusp in $E_C(T)$ close to T_C (shown in detail for DOBA-1-MPC in the inset to Fig. 1) is rather difficult to describe precisely within the GLM by using the set of fit parameters which would simultaneously describe consistently all other physical quantities. In addition to the above problems, it seems that the GLM completely fails to describe the electric-field dependence of some physical quantities such as polar ordering $\langle \cos \phi \rangle(E)$ across the $E_C(T)$ transition line (Fig. 9).

It is interesting to note that, as in the case of the $E_C(T)$ anomaly, the GLM exhibits difficulties in describing in detail also the sharp anomaly in $\Delta\varepsilon_G(T)$ just below T_C. Figure 11 shows such a Goldstone mode anomaly observed in CE8 [23]. This sharp anomaly was also observed in high-resolution dielectric experiments performed on other LC compounds such as DOBAMBC, DOBA-1-MPC, BDH762, SCE9 etc. [22,30,31].

In fact, it appears that the generalized Landau model describes qualitatively and even quantitatively well most physi-

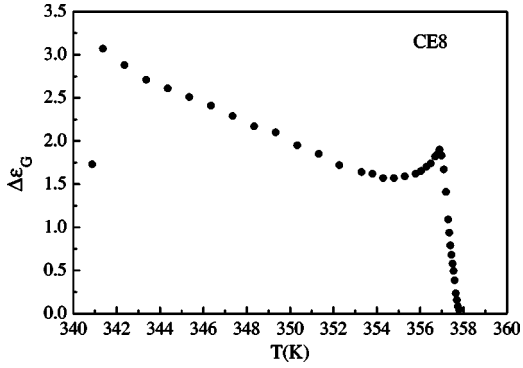

FIG. 11. Temperature dependence of the Goldstone mode dielectric intensity $\Delta\varepsilon_G(T)$ of CE8 measured in the zero-bias field by using the small ac excitation voltage [23]. Note rather sharp anomaly just below $T_C \approx 357.8$ K.

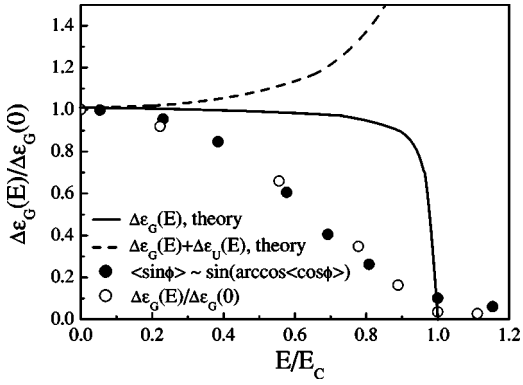

FIG. 12. Normalized intensity of the Goldstone mode $\Delta\varepsilon_G(E)/\Delta\varepsilon_G(0)$ as a function of the reduced electric field E/E_C. Solid line represents results of the calculations based on the GLM model. Also shown are calculations for the combined intensity of the Goldstone and unwinding modes (denoted by the dashed line). Solid circles represent estimation of the normalized intensity of the Goldstone mode from the $P(E)\langle\cos\phi\rangle$ experiment. Open circles represent the normalized intensity of the Goldstone mode measured directly in the dielectric experiment. Both experimental results were obtained on DOBA-1-MPC at $T_C - T = 3.2$ K.

cal quantities except those that have something to do with the deformations of the helicoidal structure; namely, all E_C transition lines, the Goldstone mode dielectric intensity $\Delta\varepsilon_G(T)$, and $P(E)$ have something to do with deformations of the helicoidal structure, i.e., either small phase deformations (approximately constant pitch) as in zero-bias-field dielectric measurements of the Goldstone mode or strong deformations (pitch changes) as in measurements of E_C and $P(E)$ where the helicoidal structure eventually gets unwound. Therefore, let us take a closer look at the GLM predictions of the dielectric response of finite-size ferroelectric liquid crystals in a bias electric field.

According to the multisoliton solution of the sine-Gordon equation [12,28]

$$K_3\theta^2\frac{\partial^2\phi}{\partial^2 z} - PE\cos\phi = 0, \tag{10}$$

the total static dielectric response related to the phase fluctuations in the bias electric field is composed of two contributions. The first contribution (Goldstone mode) corresponds to the polarization reorientation at constant period (pitch) of the helix, while the second mode (the so called unwinding mode) is related to pitch changes. The former mode should be rather fast in comparison to the latter. The field dependence of the Goldstone mode, according to the GLM based model, should slowly decrease with increasing bias field exhibiting a sharp drop just below E_C (solid line in Fig. 12). The unwinding mode, in contrast, increases strongly with increasing bias field so that the combined intensity of both modes also diverges on approaching E_C (dashed line in Fig. 12). The electric-field dependence of the Goldstone mode intensity $\Delta\varepsilon_G(E)$ of DOBA-1-MPC (shown as open circles in Fig. 12) shows a much more gradual decrease than predicted by the theory. Here, the Goldstone mode intensity was extracted from the frequency dependent complex dielectric constant data measured in the frequency range between 20 Hz and 1 MHz by applying both a static bias electric field and small oscillatory voltage signal parallel to the smectic planes, i.e., in the same way as the soft mode data (see Sec. II and related subsection).

Polarization reversal experiments could also provide a rough estimation of the normalized intensity of the Goldstone mode as a function of the bias field. It should be pointed out that the ordered part of the dielectric polarization (averaged projection of the in-plane polarization on the direction parallel to the external static bias field proportional to $\langle\cos\phi\rangle$) does not contribute anymore to the Goldstone mode; namely, a stimulating oscillatory electric field, which is also parallel to the static bias field, cannot induce phase changes any longer, i.e., rotations of the ordered part of the polarization. However, it can induce changes in the amplitude of the polarization via the electroclinic effect, which, in turn, could contribute to only the intensity of the high-frequency amplitudon (soft) mode. The intensity of the Goldstone mode should therefore be proportional to the "perpendicular component" of the dielectric polarization proportional to $\langle\sin\phi\rangle \approx \sin[\arccos(\langle\cos\phi\rangle)]$, which is not yet ordered, i.e., which averages out on the pitch distance. It is interesting to note that the normalized Goldstone mode intensity estimated from the polar ordering experiment (solid circles in Fig. 12) matches qualitatively well the normalized Goldstone mode data acquired in a classic dielectric experiment. It should also be mentioned that the above DOBA-1-MPC field-dependent Goldstone mode data agree well with the previously published field-dependent data obtained on DOBAMBC [24].

The $P(E)$ data also have another importance. It was shown that the unwinding mode would be difficult to observe by the classic dielectric method due to its slow relaxation frequency [28], which is related to the finite length of the sample along the helicoidal axis. However, in the switching current experiment performed at sufficiently high fields the helicoidal structure is forced to unwind in a rather short period of time (as observed in a stroboscopic experiment under polarizing microscope [32]). It should therefore be possible to extract the unwinding mode information from the deriva-

tive of the $P(E)$ curve, since the experimental time scale in the current reversal experiment exceeds by an order of magnitude the unwinding time of the helix (observed in the parallel stroboscopic experiment). It is obvious from Fig. 8, however, that the derivative of $P(E)$ does not show any divergence in clear disagreement with the theory (dashed curve in Fig. 12).

It appears that the above disagreements between the theory and experiments call for a different unwinding scenario as implemented in the GLM based model. In fact, the observations under a polarizing microscope published long ago [33–36] indicate that the unwinding mechanism of the helicoidal structure may indeed be different from the mechanism proposed in the GLM based model.

Under a polarizing microscope with crossed polarizers, equidistant dark and bright stripes could be observed due to rotation of the optical axis along the helicoidal axis. If the polarizer axis is properly adjusted the dark stripes could, for instance, correspond to smectic layers with the polarization oriented preferentially in the opposite direction than the external field [see schematic presentation in Fig. 13(a)]. According to the GLM model, with increasing electric bias field the soliton solution of Eq. (10) deforms increasingly strongly away from the zero-field solution described by trigonometric functions in the way that the multisoliton solution preserves periodicity. The period of this deformed structure should grow progressively and continuously with increasing electric bias field until it diverges at E_C. Consequently, under the polarizing microscope the dark stripes should become narrower and increasingly separated from each other as the pitch grows with external field approaching the critical unwinding field E_C [see schematic presentation in Fig. 13(b)]. In contrast, the polarizing microscope experiments show that in the thick planar samples the external electric field enforces the unwinding process of the helicoidal structure via mutual annihilation of pairs of $\pm 2\pi$ dechiralization lines (PDLs).

It was shown that the formation of PDLs (disclinations) is related to the existence of the unwound layers (due to surface anchoring) at the sample surfaces [33]. In thick samples these unwound layers are connected with the regular helicoidal structure deeper in the sample by means of the abovementioned $\pm 2\pi$ dechiralization lines [34]. Under the influence of the external bias electric field these pairs of dechiralization lines move and annihilate each other, thus effectively unwinding the helicoidal structure [34–36]. Those experiments together with our stroboscopic experiments show that the annihilation of the PDLs occurs nearly randomly throughout the sample [see schematic presentation in Fig. 13(c)].

At progressively increasing fields all dechiralization lines eventually disappear. The consequence of this mechanism is that typically one cannot ascribe the single period of the helicoidal structure, but instead a distribution of periods exists since large domains of various size of the homogeneous phase are formed randomly throughout the sample. This is indicated by the fact that the diffraction peaks in a light scattering experiment on the helicoidal structure—playing the role of the diffraction grating—widened and became blurred at larger bias fields, thus indicating the existence of the distribution of characteristic grating spacing. Although

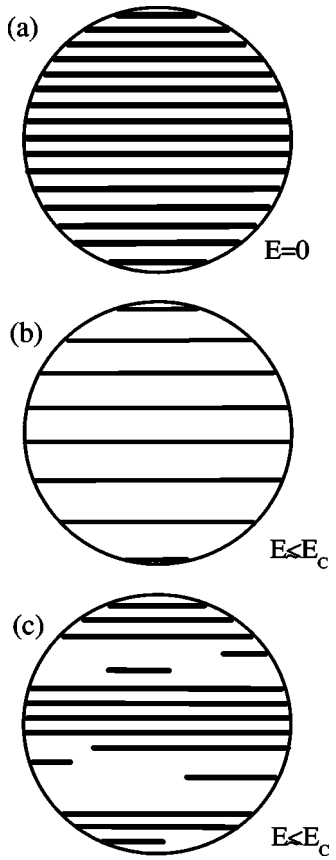

FIG. 13. Schematic presentation of the helicoidal structure as should be observed according to the theory under a polarizing microscope with crossed polarizers in zero external field (a) and in an external field just below E_C. Typical actual observation is schematically presented in (c). Here pairs of $\pm 2\pi$ disclination lines move and consequently annihilate each other. With increasing electric field the dechiralization lines progressively disappear leaving behind large domains of the helix-free homogeneous $\bar{C}$ phase.

the observed diffraction peaks widen at larger bias fields they do not completely disappear until the field approaches E_C. Therefore, it is still possible to assign the averaged period of the structure. However, there is the possibility that in some samples the dechiralization lines would disappear in such a manner that the remaining structure would adjust so as to preserve its regular periodicity. In this case perhaps there would be no broadening of the diffraction peaks. In fact, such behavior was observed in some samples at rather small electric fields below the critical one.

It is interesting to note that a stroboscopic experiment in which the electric field was switched between two very large bipolar values shows that the system does not switch as a monodomain sample, but instead goes from one helix-free homogeneous state to another homogeneous state with the reversed polarization, via a short living intermediate state with fully established helicoidal structure, which does not differ visually from the helicoidal structure observed in zero field [36]. This intermediate state was also formed and then subsequently destroyed via random creation and annihilation of the dechiralization lines. This calls for further investiga-

tion of the dynamics of the $\pm 2\pi$ disclination lines; namely, the existence of the intermediate helicoidal structure implies that in order to understand better the performance of the electro-optical switching devices based on ferroelectric LCs the unwinding mechanism via annihilation of the dechiralization lines should be understood better.

Furthermore, random disappearances of isolated dechiralization lines correspond to the random single domain switching typically observed in solid ferroelectrics. It should be stressed that the $P(E)$ curves could be well described [see solid lines in Figs. 8(a) and 8(b) and related text in Sec. III] by the "activated domain switching" ansatz (9) in which the ferroelectric domain reverses its polarization in an activated process by random jumps across some energy barrier.

The above relaxation mechanism of the helicoidal structure may also account for discrepancies between the theoretical calculations and the temperature dependence of the Goldstone mode intensity near the sharp peak just below T_C in a zero-field experiment (see Fig. 11). That is, the helicoidal structure relaxes according to the above-mentioned scenario also in the presence of some other stimulus than field, such as a change of temperature.

V. CONCLUSIONS

The experiments bring two main results. First, it appears that for physically accessible fields above E_C the E-T phase diagram can be described in a satisfactory manner within the GLM, i.e., there is no evidence for a $\overline{C_1}$ to $\overline{C_2}$ phase transition. In particular, the lack of sharp anomalies in the heat capacity and in the dielectric response at larger electric fields seems to support rather the established scenario in which the electric field above the unwinding critical field induces a state that preserves the same symmetry above and below T_C.

Second, the extended Landau model fails to describe properly the evolution of several physical quantities such as the field dependence of the Goldstone mode intensity and the polar ordering measured across the C^* to $\overline{C}$ transition line including its shape in the E-T phase diagram, i.e., the temperature dependence of the critical electric field [$E_C(T)$ line]. It is shown that the GLM model, otherwise ideal in describing phenomena of infinitely thick samples or samples with weak surface anchoring effects, cannot adequately describe the unwinding mechanism in samples of finite thickness with rather important surface anchoring effects, which are responsible for creation of $\pm 2\pi$ disclination lines. Previously published polarizing microscope experiments together with our stroboscopic experiments show that the helicoidal structure relaxes via random annihilation of the pairs of $\pm 2\pi$ disclination lines. This mechanism seems to resemble remotely the random single domain switching typically observed in classical solid ferroelectrics via detection of Barkhausen pulses.

ACKNOWLEDGMENTS

This research was supported by the Slovenian Office of Science under Program No. P1-0125 and Project No. J1-6593-0106-04.

[1] R. B. Meyer, L. Liebert, L. Strzelecki, and P. Keller, J. Phys. (France) Lett. **36**, L69 (1975).
[2] N. A. Clark and S. T. Lagerwall, Appl. Phys. Lett. **36**, 899 (1980).
[3] P. Martinot-Lagarde, R. Duke, and G. Durand, Mol. Cryst. Liq. Cryst. **25**, 249 (1981).
[4] K. Kondo, Y. Sato, H. Takezoe, A. Fukuda, and E. Kuze, Jpn. J. Appl. Phys. **20**, L871 (1981).
[5] S. Kai, M. Takata, and K. Hirakawa, Jpn. J. Appl. Phys., Part 1 **22**, 938 (1983).
[6] S. A. Rozanski and W. Kuczynski, Chem. Phys. Lett. **105**, 104 (1984).
[7] H. Takezoe, K. Kondo, K. Miyasato, S. Abe, T. Tsuchiya, A. Fukuda, and E. Kuze, Ferroelectrics **58**, 137 (1984).
[8] S. Dumrongrattana and C. C. Huang, J. Phys. (France) **47**, 2117 (1986).
[9] A. Levstik, Z. Kutnjak, B. Žekš, S. Dumrongrattana, and C. C. Huang, J. Phys. II **1**, 797 (1991).
[10] Z. Kutnjak, MS thesis, University of Ljubljana, 1991.
[11] L. Benguigui and A. E. Jacobs, Phys. Rev. E **49**, 4221 (1994).
[12] B. Kutnjak-Urbanc and B. Žekš, Phys. Rev. E **51**, 1569 (1995).
[13] B. Žekš, Mol. Cryst. Liq. Cryst. **114**, 259 (1984).
[14] A. Michelson, L. Benguigui, and D. Cabib, Phys. Rev. A **16**, 394 (1977).
[15] B. Schaub and D. Mukamel, J. Phys. C **16**, L225 (1983).
[16] C. C. Huang and J. M. Viner, Phys. Rev. A **25**, 3385 (1982).
[17] T. Carlsson, B. Žekš, C. Filipič, A. Levstik, and R. Blinc, Mol. Cryst. Liq. Cryst. **163**, 11 (1988).
[18] F. Ghoddoussi, M. A. Pantea, P. H. Keyes, R. Naik, and P. P. Vaishnava, Phys. Rev. E **68**, 051706 (2003).
[19] I. Muševič, B. Žekš, R. Blinc, T. Rasing, and P. Wyder, Phys. Rev. Lett. **48**, 192 (1982).
[20] H. Yao and C. W. Garland, Rev. Sci. Instrum. **69**, 172 (1998).
[21] Z. Kutnjak, S. Kralj, G. Lahajnar, and S. Žumer, Phys. Rev. E **68**, 021705 (2003).
[22] A. Levstik, Z. Kutnjak, C. Filipič, I. Levstik, Z. Bregar, B. Žekš, and T. Carlsson, Phys. Rev. A **42**, 2204 (1990).
[23] Z. Kutnjak, S. Kralj, and S. Žumer, Phys. Rev. E **66**, 041702 (2002).
[24] J. Pavel, M. Glogarova, and S. S. Bawa, Ferroelectrics **76**, 221 (1987).
[25] J. Pavel and M. Glogarova, Liq. Cryst. **6**, 325 (1989).
[26] I. Dahl, S. T. Lagerwall, and K. Skarp, Phys. Rev. A **36**, 4380 (1987).
[27] K. Skarp, K. Flatischler, and S. T. Lagerwall, Ferroelectrics **84**, 183 (1988).
[28] B. Žekš, T. Carlsson, I. Muševič, and B. Kutnjak-Urbanc, Liq. Cryst. **15**, 103 (1993).
[29] B. Urbanc and M. Cepic (unpublished).

[30] A. Levstik, Z. Kutnjak, C. Filipič, and B. Žekš, Ferroelectrics **126**, 139 (1992).
[31] V. Bobnar and Z. Kutnjak (unpublished).
[32] Z. Kutnjak, C. Filipič, and A. Levstik (unpublished).
[33] M. Brunet and C. Williams, Ann. Phys. (N.Y.) **3**, 237 (1978).
[34] M. Glogarova, L. Lejček, J. Pavel, V. Janovec, and J. Fousek, Mol. Cryst. Liq. Cryst. **91**, 309 (1983).
[35] M. Glogarova and J. Pavel, J. Phys. (France) **45**, 143 (1984).
[36] H. Orihara and Y. Ishibashi, Ferroelectrics **58**, 179 (1984).